UC Berkeley
UC Berkeley Previously Published Works

Title

Ice-Crystallization Kinetics in the Catalyst Layer of a Proton-Exchange-Membrane Fuel Cell

Authors

Dursch, TJ
Trigub, GJ
Lujan, R
et al.

Peer reviewed

Ice-Crystallization Kinetics in the Catalyst Layer of a Proton-Exchange-Membrane Fuel Cell

T. J. Dursch,[a,b] G. J. Trigub,[a] R. Lujan,[c] J. F. Liu,[a] R. Mukundan,[c,*] C. J. Radke,[a,d,z] and A. Z. Weber[b,*]

[a]*Chemical and Biomolecular Engineering Department, University of California, Berkeley, California 94720, USA*
[b]*Environmental Energy Technology Division, Lawrence Berkeley National Laboratory, Berkeley, California 94720, USA*
[c]*Los Alamos National Laboratory, Los Alamos, New Mexico 87545, USA*
[d]*Earth Sciences Division, Lawrence Berkeley National Laboratory, Berkeley, California 94720, USA*

Nucleation and growth of ice in the catalyst layer of a proton-exchange-membrane fuel cell (PEMFC) are investigated using isothermal differential scanning calorimetry and isothermal galvanostatic cold-starts. Isothermal ice-crystallization rates and ice-nucleation rates are obtained from heat-flow and induction-time measurements at temperatures between 240 and 273 K for four commercial carbon-support materials with varying ionomer fraction and platinum loading. Measured induction times follow expected trends from classical nucleation theory and reveal that the carbon-support material and ionomer fraction strongly impact the onset of ice crystallization. Conversely, dispersed platinum particles play little role in ice crystallization. Following our previous approach, a nonlinear ice-crystallization rate expression is obtained from Johnson-Mehl-Avrami-Kolmogorov (JMAK) theory. A validated rate expression is now available for predicting ice crystallization within water-saturated catalyst layers. Using a simplified PEMFC isothermal cold-start continuum model, we compare cell-failure time predicted using the newly obtained rate expression to that predicted using a traditional thermodynamic-based approach. From this comparison, we identify conditions under which including ice-crystallization kinetics is critical and elucidate the impact of freezing kinetics on low-temperature PEMFC operation. The numerical model illustrates that cell-failure time increases with increasing temperature due to a longer required time for ice nucleation. Hence, ice-crystallization kinetics is critical when induction times are long (i.e., in the "nucleation-limited" regime for $T > 263$ K). Cell-failure times predicted using ice-freezing kinetics are in good agreement with the isothermal cold-starts, which also exhibit long and distributed cell-failure times for $T > 263$ K. These findings demonstrate a significant departure from cell-failure times predicted using the thermodynamic-based approach.
© 2013 The Electrochemical Society. [DOI: 10.1149/2.004403jes] All rights reserved.

Proton-exchange-membrane fuel cells (PEMFCs) show promise in automotive applications because of their high efficiency, high power density, and potentially low emissions. To be successful in automotive applications, PEMFCs must permit rapid startup with minimal energy from sub-freezing temperatures, known as cold-start. In a PEMFC, reduction of oxygen to water occurs in the cathode catalyst layer (cCL). Under subfreezing conditions, water solidifies and hinders access of gaseous oxygen to the catalytic sites in the cCL, severely inhibiting cell performance and potentially causing cell failure.[1–3] Elucidation of the mechanisms and kinetics of ice formation within the cCL is, therefore, critical to successful cell startup and high performance at low temperatures.

Because of degradation and cell failure under subfreezing conditions, much attention has been given to understanding cold-start fundamentals. To date, experiments predominantly focus on characterizing overall low-temperature cell performance.[1–7] In recent years, however, in-situ visualization and detection of ice formation within PEMFC porous media has progressed.[7–14] Visualization methods include neutron radiography,[8,9] environmental scanning electron microscopy,[10] visible imaging,[11–13] and latent-heat detection with infrared thermography.[11,12] In all cases, generation of by-product water was observed in the subcooled state, particularly between –2 and –20°C. Although the generated liquid water did not freeze instantaneously, crystallization kinetics and its dependence on subcooling were not investigated.[7–13]

Several PEMFC numerical cold-start models have also been recently developed.[14–19] Currently, however, no models include ice-crystallization kinetics, and consequently, do not account for sub-cooled liquid.[14–19] Commonly, models assume that product water vapor instantaneously solidifies when the vapor partial pressure exceeds the saturation value.[14–16] As a result, they do not account for liquid water within the PEMFC. More recently, Jiao et al.[17] and Balliet et al.[18,19] extended cold-start models to include vapor, liquid, and solid

phases of water within the PEMFC. The freezing point of ice within the GDL, cCL, and PEM is based on a characteristic pore size using the Gibbs-Thomson equation. Further, the ice-formation rate, R_I, is assumed linear with liquid-water saturation[18]

$$R_I \approx k_f S_L \qquad [1]$$

where k_f is the freezing rate constant (e.g., see Eq. 14 in Balliet et al).[18] Although the models include liquid water,[17–19] they currently invoke thermodynamic-based freezing and circumvent ice-crystallization kinetics.

In this work, we measure isothermal ice-crystallization kinetics within PEMFC catalyst layers. Experimental ice-nucleation rates and ice-crystallization kinetics are obtained as functions of subcooling from isothermal differential-scanning-calorimetry (DSC) heat-flow measurements in water-saturated cCLs. Following our previous approach,[20,21] we determine a rate expression for ice crystallization within cCLs. To validate ice-crystallization kinetics within PEMFCs, we further measure and predict cell-failure time during isothermal galvanostatic cold-start. Using a simplified PEMFC isothermal cold-start continuum model, we compare cell-failure time predicted using the newly obtained rate expression to that predicted using a traditional thermodynamic-based approach (i.e., Eq. 1). From this comparison, we identify conditions under which including ice-crystallization kinetics is critical and elucidate the impact of freezing kinetics on low-temperature PEMFC operation.

Materials and Methods

Catalyst preparation.— Catalyst inks were prepared following Huang et al.[22] Inks were made by mixing 20-wt% Pt on Vulcan XC72 carbon black (Pt/C) (Sigma Aldrich, St. Louis, MO, Cat. No.: 738549–1 G) with a 5-wt% Nafion solution (Sigma Aldrich, Cat. No.: 70160–25 ML) in a 5:2 mass ratio (Carbon:Nafion). After stirring for 15 min, 1-M tetrabutylammonium hydroxide (TBAOH) (Sigma Aldrich, Cat. No.: 86854–100 ML) and glycerol (Sigma Aldrich, Cat. No.: G5516–100 ML) were added in a mass ratio of 1:20:20 (glycerol:TBAOH:Nafion). The resulting solution was stirred overnight.

*Electrochemical Society Active Member.
[z]E-mail: radke@berkeley.edu

Following the same procedure, catalyst inks were prepared for three other carbon supports (containing no Pt): Black Pearls BP120, BP460, and BP800 (Cabot Corporation, Boston, MA). Additionally, catalyst inks were made for Vulcan XC72 without Pt and with varying Carbon:Nafion mass ratios (5:1, 5:4, and 5:8) for BP800 and Vulcan XC72. Unless otherwise stated, the Carbon:Nafion mass ratio is 5:2.

In all cases, catalyst inks (approximately 6 μL) were pipetted directly into 20-μL aluminum DSC pans (PerkinElmer Inc., Waltham, MA) and dried at 298 K under vacuum (4.7 kPa) to avoid cracking caused by rapid solvent evaporation. Dried samples were then saturated with Ultrapure Milli-Q (Millipore, Billerica, MA) distilled/deionized water in a home-built vacuum chamber for 1 h at 4.7 kPa. Following evacuation, excess surface water was removed by lightly blotting with Fisherbrand weighing paper (Fisher Scientific, Pittsburgh, PA). Water content was determined gravimetrically; measured values were consistent with integrated peak areas generated from DSC. Water loss by evaporation during DSC experiments was negligible. All catalyst water saturations are calculated from measured water contents to be between 78% and 94%, corresponding to typical porosities of 0.5 and 0.6, respectively.[5,18,19,23]

Differential scanning calorimetry.— A PerkinElmer 6000 DSC (PerkinElmer Inc., Waltham, MA) with a liquid-nitrogen chiller measured heat-flow rate from the sample over time. The DSC was calibrated as described previously.[20] Nitrogen served as the purge gas at a flow rate of 20 mL/min. Isothermal crystallization was carried out from 240 to 273 K. Water-saturated catalyst samples were placed into the DSC at 300 K and cooled to the desired temperature at 105 K/min. A rapid cooling rate was chosen to reach the isothermal freezing temperature well before the onset of crystallization. Samples were then held at the subcooled temperature until crystallization was complete. Experiments were performed at various subcoolings, $\Delta T = T_o - T$, defined as the magnitude of the difference in the temperature of freezing and 273 K.

Isothermal cold-start.— Membrane electrode assemblies (MEAs) were provided by Ion Power (Ion Power, Inc., New Castle, DE). MEAs consisted of a DuPont Nafion XL membrane, a TEC10EA40E cathode, and a TEC10V20E anode with 0.15 and 0.07 mg/cm² Pt loading, respectively. Ion Power purchased the cathode and anode catalysts from Tanaka Kikinzoku Kogyo K.K. (Tanaka Kikinzoku Kogyo K.K., Tokyo, Japan) and mixed them with a Nafion solution to form an ink that was then painted on a web prior to transfer to the membrane. MEAs were assembled in single 50-cm² quad-serpentine fuel-cell hardware with cooling loops machined into both end plates. Cells were tested on a Fuel Cell Technologies testing stand (Fuel Cell Technologies, Inc., Albuquerque, NM) and cooled using a Neslab ULT-80 bath circulator.

Prior to each isothermal cold-start experiment, cells were conditioned at a current density of 1000 mA/cm² at 353 K and 100% relative humidity. Following, cathode and anode flow channels were purged with 1000 mL/min of nitrogen gas for 30 s to prevent water from forming ice and clogging the flow fields. Cells were then cooled to the desired isothermal freezing temperature and equilibrated at that temperature for 30 min. Isothermal cold-start experiments were carried out with 500 sccm of dry hydrogen and air. Following an initial current ramp of 0.4 mA/cm²/s, current of 20 mA/cm² was applied until the cell voltage decayed to 0 mV. The cells were then heated to 353 K for characterization, and cycling was repeated.

Experimental Results

Ice-crystallization kinetics.— Figure 1 shows a typical exotherm of heat flow and sample temperature versus time for a water-saturated Vulcan XC72 catalyst. The sample was cooled at 105 K/min to 257 K (i.e., $\Delta T = 16$ K), where isothermal crystallization commenced (point A in Figure 1). Heat flow due to liberation of the enthalpy of crystallization from point A is evident until a minimum is observed at point B, after which crystallization slows significantly until complete
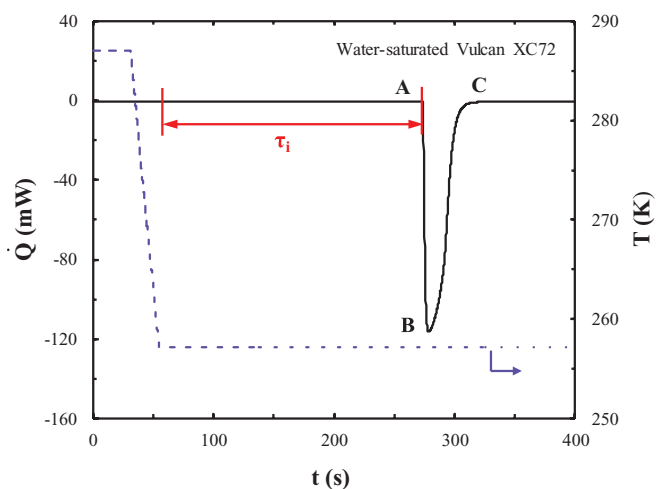

Figure 1. Typical isothermal DSC cooling exotherm of a water-saturated Vulcan XC72 catalyst at 257 K. The dashed line corresponds to the sample temperature, T, whereas the solid line represents heat-flow rate, $\dot{Q}$. The symbol τ_i labels the induction time. A-C label the onset, extremum, and completion of water freezing, respectively.

crystallization at point C. To obtain the gas-free ice volume fraction within the catalyst pores as a function of time, $\phi(t)$, crystallization exotherms were integrated from point A to point C, according to[20,21]

$$\phi(t) = \frac{\int_0^t \dot{Q}(t)dt}{\int_0^\infty \dot{Q}(t)dt} \qquad [2]$$

where $\dot{Q}(t)$ is heat-flow rate from the DSC. Crystallization is preceded by an induction time, τ_i, defined as the time elapsed between the sample temperature becoming isothermal and the onset of the crystallization peak (point A), about 225 s in Figure 1.

Figure 2 displays number-average induction time, $\bar{\tau}_i$, as a function of subcooling, ΔT, for five water-saturated catalysts: 20 wt% Pt on Vulcan XC72 (triangles), Vulcan XC72 without Pt (squares), BP120 (inverted triangles), BP460 (diamonds), and BP800 (circles). Symbols denote average-τ_i measurements for a minimum of 25 experiments.
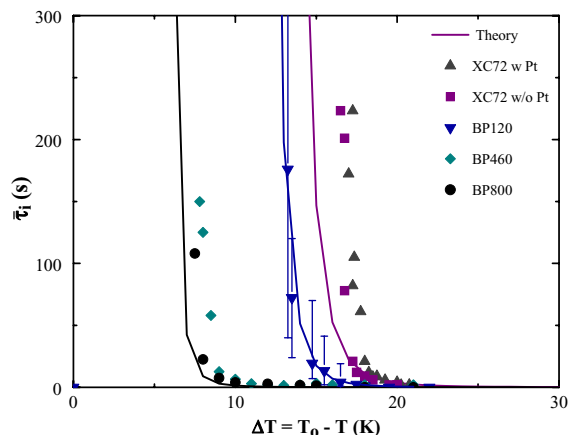

Figure 2. Isothermal number-average induction time, $\bar{\tau}_i$, as a function of subcooling, ΔT, for five PEMFC catalysts. Symbols correspond to 20-wt% Pt on Vulcan XC72 (triangles), Vulcan XC72 without Pt (squares), BP120 (inverted triangles), BP460 (diamonds), and BP800 (circles). Example error bars indicate the maximum range of observed τ_i. Solid lines are predictions of $\tau_i(\Delta T)$ from classical nucleation theory using Eqs. 5 and 6.

(a) Figure 3 top panel
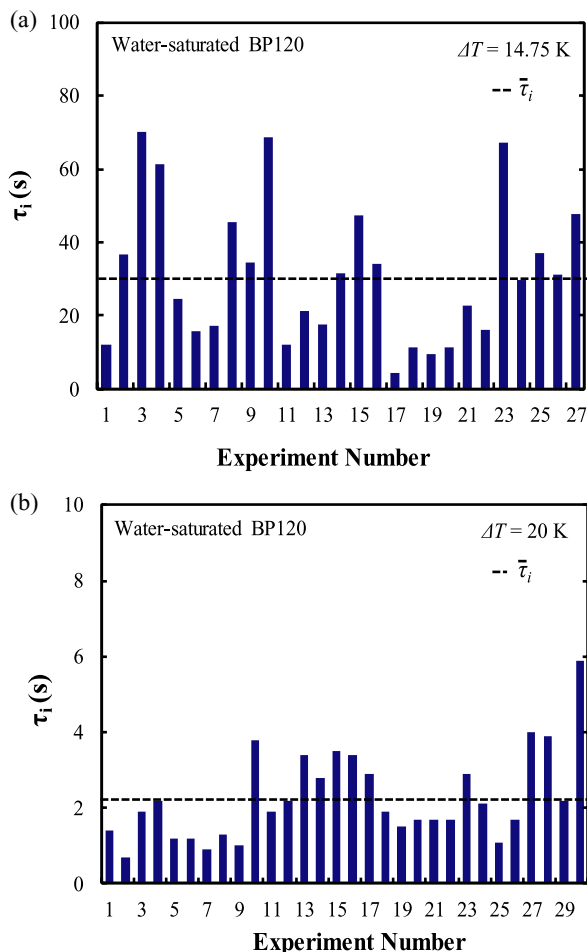

(b) Figure 3 bottom panel

Figure 3. 25 induction-time measurements at a subcooling of (a) 14.75 K and (b) 20 K for BP120. Horizontal dashed lines indicate the number-average induction time, $\bar{\tau}_i$.

Figure 4. Isothermal freezing kinetics for five PEMFC catalysts. Symbols denote 20 wt% Pt on Vulcan XC72 (triangles), Vulcan XC72 without Pt (squares), BP120 (inverted triangles), BP460 (diamonds), and BP800 (circles). Filled symbols correspond to a subcooling of 17.5 K, whereas open symbols (circles) correspond to a subcooling of 11 K. Solid and dashed lines are predictions of $\phi(t)$ using Eqs. 3 and 4, at subcoolings of 17.5 and 11 K, respectively.

Vulcan XC72 (triangles), Vulcan XC72 without Pt (squares), BP120 (inverted triangles), BP460 (diamonds), and BP800 (circles). Filled symbols correspond to a subcooling of 17.5 K, whereas open symbols (circles) correspond to a subcooling of 11 K. Solid and dashed lines are predictions of $\phi(t)$ from Johnson-Mehl-Avrami-Kolmogorov (JMAK) theory at $\Delta T = 17.5$ K and 11 K, respectively, as discussed below. At each subcooling, τ_i was subtracted from the total time so that all curves are compared on a single time scale. Complete ice-crystallization times (taken when $\phi(t) = 0.99$) are 13.3, 13.7, 22.0, and 24.1 s for BP460, BP800, BP120, and Vulcan XC72 at 17.5 K, respectively. Similar to Figure 2, Figure 4 illustrates that the carbon-support material appreciably impacts ice-freezing kinetics. Likewise, nearly identical $\phi(t)$ for Vulcan XC72 with and without platinum demonstrates that dispersed platinum does not significantly affect the kinetics of ice-crystallization. As ΔT decreases from 17.5 K to 11 K for BP800, complete ice-crystallization times increase from 13.3 to 27.7 s. This result reiterates that subcooling, ΔT, is the driving force for ice crystallization.[20]

Typical error bars for BP120 are discussed below. Solid lines are drawn according to classical nucleation theory (CNT), as discussed later. Several features are salient. In all cases, $\bar{\tau}_i$ decreases with increasing ΔT, as expected.[20,21,24] $\bar{\tau}_i$ measurements for Vulcan XC72 are similar to those for BP120 and BP460/800, but are shifted to larger ΔT by about 3 and 8 K, compared to those for BP120 and BP460/800, respectively. This result indicates that the specific carbon-support material impacts the onset of ice crystallization. Similar $\bar{\tau}_i$ measurements for Vulcan XC72 with and without added platinum (compare triangles and squares) at nearly all ΔT reveals that dispersed platinum particles, with diameters ranging from 3–5 nm,[10] play little role in ice crystallization at typical loadings.

Example error bars in Figure 2 indicate the maximum range of observed τ_i. For all catalysts, τ_i was measured repeatedly to investigate the statistical nature of ice crystallization and to obtain pseudo-steady-state ice-nucleation rates, as discussed below. Representative results for BP120 are shown in Figure 3. Figure 3 displays at least 25 induction times measured at subcoolings of (a) 14.75 K and (b) 20 K for BP120, where the horizontal dashed line indicates the number-average induction time, $\bar{\tau}_i$. For both subcoolings, ΔT, τ_i generally lies below the mean with intermittent excursions to long times. Increased subcoolings result in narrower τ_i-distributions. Due to the stochastic nature of ice nucleation, τ_i measurements follow a Poisson distribution, as discussed elsewhere.[20,21,24]

Figure 4 shows ice-crystallization kinetics, $\phi(t)$ versus t, calculated from Eq. 2 for the five water-saturated catalysts in Figure 2 (for specific samples with $\tau_i \approx \bar{\tau}_i$). Symbols denote 20- wt% Pt on
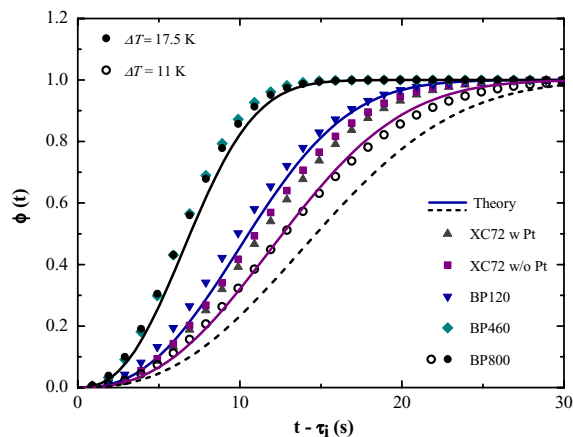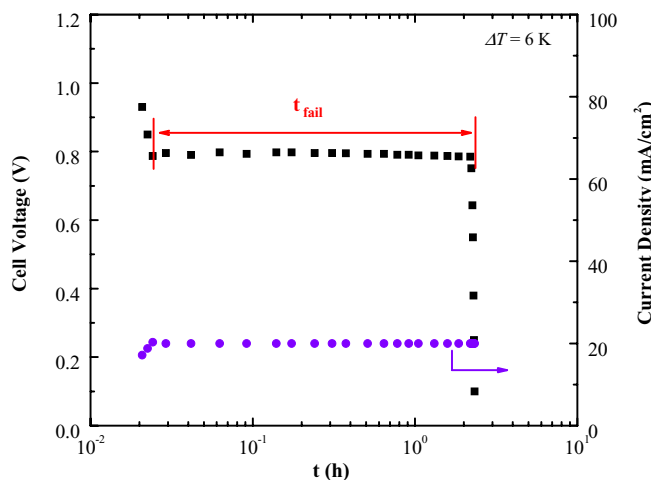

Figure 5. Typical evolution of MEA cell voltage during isothermal galvanostatic cold-start from 267 K. Squares denote cell voltage, whereas circles represent current density. The symbol t_{fail} labels the cell-failure time.
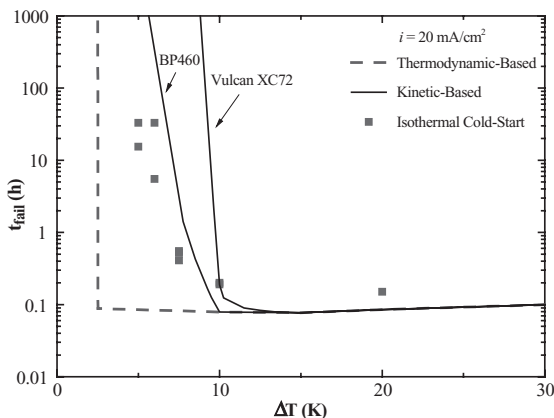
Figure 6. MEA-cell-failure time, t_{fail}, for isothermal galvanostatic start-up as a function of subcooling, ΔT, at a current density of 20 mA/cm². Solid lines are calculated using ice-crystallization kinetics for BP460 and Vulcan XC72 (with 20 wt% Pt) catalysts in a PEMFC continuum model (Appendix A). The dashed line is calculated using a typical thermodynamic-based rate expression (i.e., Eq. 1).[18]
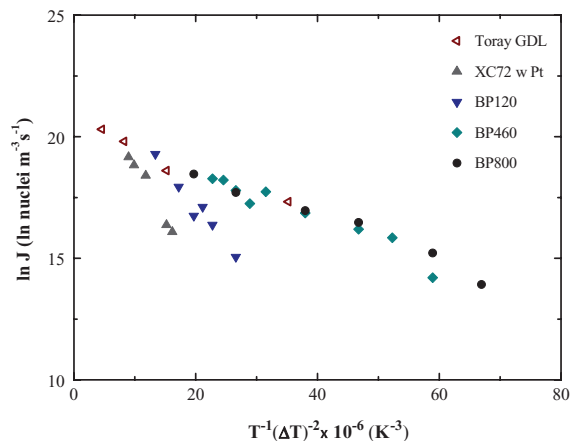

Figure 7. Logarithm of the nucleation rate, J, in units of nuclei/m³/s as a function of $T^{-1}(\Delta T)^{-2}$ for a Toray gas-diffusion layer (open symbols) and four PEMFC catalysts (filled symbols). Filled symbols represents 20-wt% Pt on Vulcan XC72 (triangles), BP120 (inverted triangles), BP460 (diamonds), and BP800 (circles).

Isothermal cold-start.— Figure 5 shows a typical evolution of MEA cell voltage (squares) during isothermal cold-start from a sub-cooling of 6 K at a current density (circles) of 20 mA/cm². Initially, cell voltage decreases from 1.0 to 0.8 V during the current ramp of 0.4 mA/cm²/s. Following a constant current density of 20 mA/cm², cell voltage remains constant until failure (i.e., when cell voltage rapidly decreases to 0 mV) as a result of ice formation within the cathode.[1–19,35] We define the cell-failure time, t_{fail}, as the time elapsed between the onset of constant cell voltage and 0 mV. We do not include the 30-min stabilization period when determining measured t_{fail}. To demonstrate applicability of ice-freezing kinetics to PEMFC cold-start, isothermal t_{fail} was measured as a function of ΔT.

Figure 6 plots isothermal t_{fail} versus ΔT at a current density of 20 mA/cm². Solid and dashed lines are discussed below in the model section and Appendix A. As ΔT increases, t_{fail} decreases substantially due to a shorter time required for ice nucleation (i.e., decreased $\bar{\tau}_i(\Delta T)$ in Figure 2). For example, t_{fail} decreases from 15.5 and 33 h to 0.19 and 0.2 h for an increase in ΔT from 5 to 10 K, respectively. The variance (not shown) between repeated t_{fail} measurements also decreases significantly with increasing ΔT, suggesting that stochastic nucleation events are critical at low subcoolings. This finding is consistent with narrowing τ_i-distributions for increased ΔT (compare Figure 2a and Figure 2b). Since a single induction time corresponds to a given cell-failure time, t_{fail} values are similarly distributed. Our measured isothermal cell-failure times are similar to those obtained by Oberholzer et al.,[8] who observed a Poisson distribution of MEA-cell-failure times during isothermal galvanostatic cold-start from 258 to 268 K using neutron imaging.

Ice-Crystallization Rate Expression

To obtain a predictive ice-crystallization rate equation, $\phi(t)$ and $\bar{\tau}_i$ must be specified a priori. Following our previous development,[20] we employ Johnson-Mehl-Avrami-Kolmogorov (JMAK) theory and classical nucleation theory (CNT). We summarize the procedure below. Additional detail is available elsewhere.[20]

Within the JMAK framework,[20,25–28] $\phi(t)$ is determined by a convolution integral over nucleation and growth rates (see Eq. 4 of Dursch et al.)[20] For spherical, heat-transfer-limited growth under isothermal conditions in a closed system, the convolution integral reduces considerably. In this case, $\phi(t; T)$ is given by[20,21]

$$\phi(t;T) = 1 - \exp\left[-k(T)[t - \bar{\tau}_i(T)]^{5/2}\right] \quad [3]$$

with

$$k(T) = \frac{64\pi}{15} g(\theta) J(T) \eta_o^3(T) \alpha_L^{3/2}, \quad [4]$$

where α_L is liquid thermal diffusivity, $J(T)$ is the pseudo-steady-state nucleation rate, $\eta_o(T)$ is a dimensionless temperature-dependent growth parameter (see Eq. 9 of Dursch et al.,)[20] θ is the contact angle of the ice/water/substrate triple line, and $g(\theta) = (2+\cos\theta)(1-\cos\theta)^2/4$ for heterogeneous nucleus growth on a flat surface. Eqs. 3 and 4 predict the ice-crystallization rates, $R_I(t; T, \phi) = \partial\phi(t;T)/\partial t$,[21] once the unknowns $J(T)$, θ, and $\bar{\tau}_i(T)$ are specified.

To obtain $\bar{\tau}_i(T)$, the definition suggested by Kaschiev[29] is adopted

$$\bar{\tau}_i(T) = \frac{1}{J(T)V_o} + \tau_g(T), \quad [5]$$

where V_o is liquid volume of a water-saturated cCL. The first term on the right of Eq. 5 is the expectation time for the appearance of a critical nucleus while the second term is the time required for critical nuclei to form and grow to a size detectable by the DSC. For spherical, heat-transfer-limited growth[24,29] $\tau_g(T) = (15\omega/64\pi g(\theta)J(T)\eta_o^3(T)\alpha_L^{3/2})^{2/5}$, where ω, an instrument-specific constant, is 0.0173 for our DSC.[21] Thus, estimation of $\bar{\tau}_i(T)$ requires both $J(T)$ and θ.

Following our previous work,[20,21] $J(T)$ is obtained from repeated τ_i measurements at a minimum of five subcoolings (e.g., see Figure 3). To acquire $J(T)$, a Poisson distribution is fit to measured τ_i probability distributions obtained from the repeated τ_i measurements.[20,24] CNT specifies the temperature-dependence of J[20,30,31]

$$J(T) = A \exp\left[-\frac{B}{T(\Delta T)^2}\right]. \quad [6]$$

Eq. 6 indicates that a plot of $\ln J$ versus $T^{-1}(\Delta T)^{-2}$ produces a straight line with an intercept $\ln A$ and slope $-B$. Figure 7 confirms this behavior for the four PEMFC catalysts shown in Figure 2 (filled symbols). A Toray gas-diffusion layer (GDL) (open symbols) is included for comparison.[20] In all cases, $\ln J$ versus $T^{-1}(\Delta T)^{-2}$ is linear with $0.91 < R^2 < 0.99$, where R^2 is the square of the Pearson correlation coefficient. Obtained ice-nucleation-rate parameters, A and B in Eq. 6, are provided in Table I, and their physical significance is discussed in Appendix B.

With $J(T)$ specified, Eqs. 3–6 provide a predictive ice-crystallization rate valid within PEMFC cCLs. In all subsequent calculations, $\alpha_L = 1.4 \times 10^{-7}$ m²/s and $\theta = 60°$ and $110°$ for BP460/BP800 and XC72/BP120, respectively. Values of θ are discussed in detail in Appendix B. With these independently determined parameters, lines

Table I. Ice-Nucleation Rate Parameters.

cCL/GDL	A ($\times 10^{-8}$ nuclei m^{-3} s^{-1})	B ($\times 10^{-4}$ K^3)
Vulcan XC72	112.7	40.3
BP120	287.0	44.1
BP460	9.0	12.8
BP800	6.6	10.6
Toray GDL	[a]7.9	[a]9.4

[a]From Dursch et al.[20]

in Figures 2 and 4 predict $\bar{\tau}_i(T)$ and $\phi(t; T)$ for three PEMFC catalysts: BP800, BP120, and 20-wt% Pt on Vulcan XC72. In all cases, we neglect separate ice formation within the ionomer, since the fraction of freezable water is negligible compared to that in the liquid-filled voids.[32] For clarity, predictions for BP460 and Vulcan XC72 without Pt are omitted. Agreement between theory and experiment is good. Through independent assessment of $J(T)$, $\eta_o(T)$, and $\tau_g(T)$, the temperature dependences of both $\bar{\tau}_i$ and $\phi(t)$ are correctly captured. Importantly, lines in Figure 4 at $\Delta T = 17.5$K show that complete ice-crystallization times are shorter for BP800 and BP120 than those for Vulcan XC72 due to an increased ice-nucleation rate (i.e., larger A and/or smaller B in Table I) and consequently, a decreased $\bar{\tau}_i$.

Isothermal PEMFC Cold-Start Model

Continuum model.— Eqs. 3–6 provide an ice-crystallization rate expression valid within PEMFC catalyst layers. To investigate the importance of ice-crystallization kinetics, we compare predicted t_{fail} with the newly obtained rate expression relative to that predicted using a traditional thermodynamic-based approach (e.g., Eq. 1)[17–19] in a simplified isothermal PEMFC cold-start continuum-finite-difference model (see Appendix A).

Figure 8 illustrates the simplified 1-D geometry of the PEMFC. Dashed lines outline the spatial domain (i.e., we consider only the cCL and cGDL). Symbols a and c label the anode and cathode, respectively. We neglect water transport and subsequent freezing within the anode, since the diffusivity of water in a PEM is negligible at subfreezing temperatures.[5] Meng,[14] Mao et al.,[15,16] Jiao et al.,[17] and Balliet et al.[18,19] give more detailed 2-D and 3-D cold-start models including thermodynamic-based ice formation in both the anode and cathode. Here, we illustrate the importance of ice-crystallization kinetics.

Continuum energy and mass conservation balances are written in the cCL and cGDL for gas (G), liquid (L), and ice (I). Appendix A outlines the PEMFC cold-start numerical model. It is similar to those of Mao et al.[15,16] and Balliet et al.,[18,19] but with important differences in the underlying physics for the ice-crystallization rate, R_I. In the

Figure 8. Schematic and boundary conditions for the simplified 1-D PEMFC cold-start model. Dashed lines represent the modeling domain. Subscript x indicates partial differentiation. Prefix letters a and c denote the anode and cathode, respectively.

Table II. Model Parameters.

Parameter	cCL	cGDL
ε_o	0.6 [18]	0.8 [20]
$\overline{\rho\hat{C}}_P$ (kJ m^{-3} K^{-1})	990 [19]	970 [19]
k_T (W m^{-1} K^{-1})	1.2 [18]	1.5 [18, 34]
k_o (m^{-2})	1.6×10^{-15} [19]	3.4×10^{-12}[19]
η_s (V)	[a]0.55	–
Π(V)	-0.012 [19]	–
U_{eff}, U (W m^{-2} K^{-1})	90 [18]	100 [18]
$A \times 10^{-8}$ (nuclei m^{-3} s^1)	9 to 112.7	7.9 [20]
$B \times 10^{-4}$ (K^3)	12.8 to 40.3	9.4 [20]

[a]calculated from measured cell voltage in Figure 5.
*gas, liquid water, and ice physical properties are taken at 298 K and 1 atm.

current study, the ice-crystallization rate depends on the kinetics of ice nucleation and growth rather than on ice/water phase equilibria. Following our previous work,[21] the ice-generation rate under pseudo-isothermal conditions, $R_I(\bar{T}_C, \phi)$ ((generated ice volume)/(water plus ice volume)/time) is given by

$$R_I(\bar{T}_C, \phi) = k(\bar{T}_C)^{2/5}[1 - \phi][-\ln(1 - \phi)]^{3/5} \quad \text{for } t \geq \bar{\tau}_I, \quad [7]$$

where $\bar{T}_C$ is number-average crystallization temperature, $\bar{\tau}_I$ is number-average non-isothermal induction time, ϕ is gas-free volume fraction of ice within the pores defined by $\phi \equiv S_I/(S_I + S_L)$, and $k(\bar{T}_C)$ is given by Eq. 4, but evaluated at the number-average crystallization temperature, $\bar{T}_C$.[21] Eq. 7 applies only for $t > \bar{\tau}_I$ (i.e., the non-isothermal induction time). $\bar{\tau}_I$ is given by[21]

$$\int_0^{\bar{\tau}_I} \frac{dt}{\bar{\tau}_i(T)} = 1, \quad [8]$$

where $\bar{\tau}_i(T)$ follows from the first term on the right of Eq. 5, as well as Eq. 6. We note that for calculation of $\bar{\tau}_i(T)$ during PEMFC cold-start, the instrument-specific growth term does not apply. In Eq. 5, $\bar{\tau}_i(T)$ depends on liquid volume in either the cCL or GDL, V_o. To eliminate the volume-dependence of $\bar{\tau}_i(T)$ in the continuum MEA-cold-start model, we evaluate $\bar{\tau}_i(T)$ for large V_o (i.e., the fastest onset of ice crystallization). The approximation of "large volume" is valid since for small ΔT, $\bar{\tau}_i(T)$ depends only on $J(T)$ and not on V_o.[21]

Coupled, nonlinear differential-algebraic equations (Eqs. 4–8 and A1–A6) are solved simultaneously subject to the boundary conditions provided in Figure 8. U_{eff} is the overall effective heat-transfer coefficient that includes heat conduction through the anode and external convection. In all cases, temperature is uniform at the isothermal ambient subcooling, $\Delta T = 273.15 - T_a$, where T_a is the ambient temperature. Similar to Jiao et al.[17] and Balliet et al.,[18,19] the initial liquid-water saturation, S_{Lo}, is 0.34 and 0.22 in the cCL and cGDL, respectively. In both the cCL and cGDL, initial gas pressure is uniform at 101.3 kPa. Equations are solved numerically in Matlab R2010a (The Math Works Inc., Natick, MA) using finite differencing and Newton iteration to resolve nonlinearities with a tolerance of 10^{-7}, a time step of 10^{-2} s, and 50 mesh elements. A Thomas-algorithm inversion scheme BAND(j) solves the resulting tridiagonal matrices.[33] All model parameters are reported in Table II.

Model results.— Figure 9 displays typical calculated liquid-water saturations, S_L, as a function of time, t, at the coldest boundaries of the cCL ($x = L$) and cGDL ($x = 0$) at equal subcoolings, ΔT, of 10 K at $x = 0, L$ and $i = 20$ mA/cm^2. Solid lines reflect the proposed ice-crystallization kinetic model (i.e., Eqs. 4–8) for the Vulcan XC72 catalyst and the Toray cGDL in Table I. Initially, S_L slightly increases in both the cCL and cGDL as a result of water generation in the cCL and subsequent migration to the cGDL due to a gradient in capillary pressure. S_L continues to increase until crystallization first commences
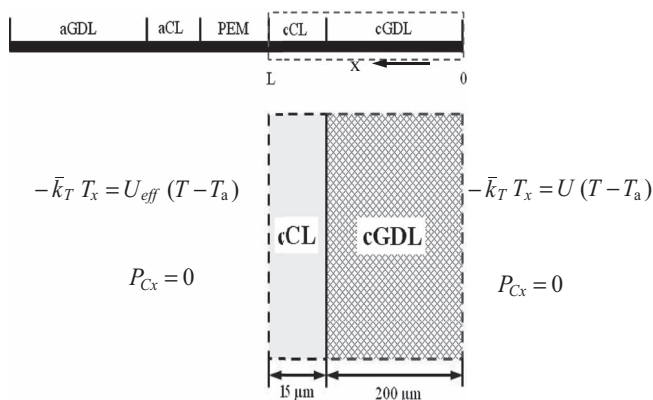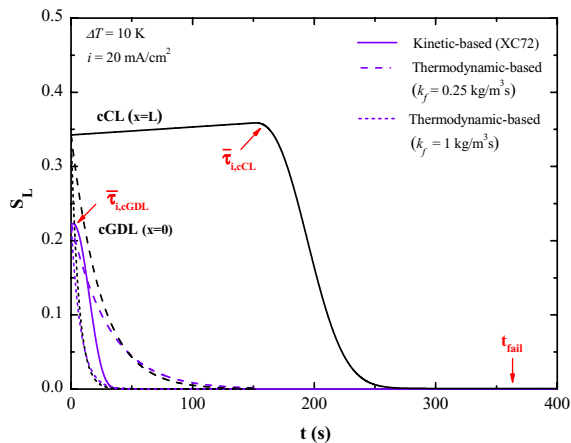
Figure 9. Calculated liquid-water saturation, S_L, as a function of time, t, at the coldest boundary of the cCL ($x = L$) and cGDL ($x = 0$) for equal subcoolings, ΔT, of 10 K. Solid lines are calculated using ice-crystallization kinetics for the Vulcan XC72 cCL and the Toray cGDL. Dashed and dotted lines are predicted using Eq. 1 with $k_f = 0.25$ and 1 kg/m³s, respectively.[18] Symbols $\bar{\tau}_{I,cGDL}$ and $\bar{\tau}_{I,cCL}$ label the number-average non-isothermal induction times in the cCL and the cGDL, respectively. The symbol t_{fail} labels the predicted MEA-cell-failure time.

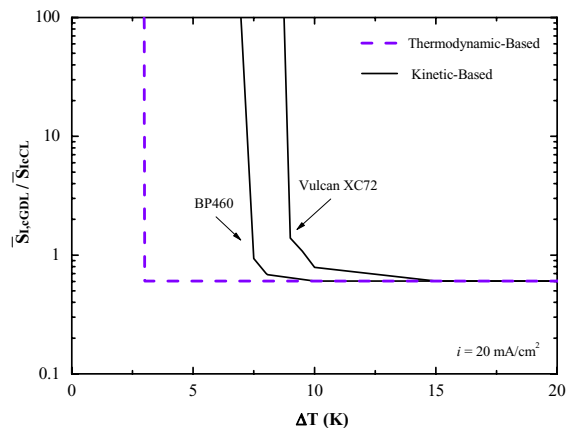**Figure 10.** Ratio of the average ice saturation in the cGDL to that in the cCL, $\bar{S}_{I,cGDL}/\bar{S}_{I,cCL}$, as a function of subcooling, ΔT, at a current density of 20 mA/cm². Solid lines are calculated using ice-crystallization kinetics in the BP460 and Vulcan XC72 cCLs and the Toray cGDL. The dashed line is calculated using a typical thermodynamic-based rate expression (i.e., Eq. 1).[18]

in the cGDL at the number-average non-isothermal induction time, $\bar{\tau}_{I,cGDL}$, where liquid water rapidly transforms into ice.[20,21,34] In the cCL, $\bar{\tau}_{I,cCL}$ is considerably longer than that in the cGDL due to slower ice nucleation rates (see Table I). Consequently, S_L increases over a longer time period prior to freezing. S_L and T profiles at given times are omitted, as both are essentially uniform due to a small Biot number ($Bi = 0.002$) and a fast time-scale for water movement.

Conversely, dashed and dotted lines in Figure 9 are calculated using a thermodynamic-based approach (i.e., Eq. 1).[18] Dashed and dotted lines correspond to $k_f = 0.25$ and 1 kg/m³s, respectively.[18] In this approach, freezing begins once the local liquid temperature is less than the equilibrium freezing temperature, T_o. For $\Delta T = 10$ K, T is well below T_o within the cCL (270.2 to 271.1 K)[11] and within the cGDL (273.0 K).[11,35] Accordingly, S_L decreases abruptly in both cases due to nearly immediate freezing. In this calculation, we neglect the relatively narrow pore-size distributions of the cGDL or cCL.[18,19] Figure 9 highlights the importance of $\bar{\tau}_I$ for forestalling freezing especially in the cCL.

The likelihood of successful cold-start depends strongly on temperature through $\bar{\tau}_I$. Thus, to elucidate those conditions for which including ice-crystallization kinetics is critical, we examine isothermal cell-failure time for various subcoolings, ΔT. We define a cell-failure time, t_{fail}, as the time when ice reaches a critical saturation, S_{Ifail}, thereby choking the cell.[34] In all cases, S_{Ifail} is taken as 0.38 and 0.55 in the cCL and cGDL, respectively. In the cCL, $S_{Ifail} = 0.38$ is obtained from a fit of measured cell voltage versus time at $\Delta T = 10$ K and $i = 20$ mA/cm². In the cGDL, however, $S_{Ifail} = 0.55$ is taken as the saturation when the effective oxygen diffusion coefficient reaches a limiting value,[36,37] taken as 0.03 in all cases. A partially ice-saturated cCL and cGDL (i.e., $S_{Ifail} < 1$) at cell failure are consistent with experimental observation.[3,4,38]

Solid and dashed lines in Figure 6 compared predicted to measured (symbols) t_{fail} versus ΔT for an isothermal galvanostatic cold-start. Solid lines correspond to ice-crystallization kinetics (i.e., Eqs. 4–8) for two cCL carbon-support materials with considerably different ice-crystallization kinetics: Vulcan XC72 and BP460. The dashed line is predicted using a traditional thermodynamic-based approach with $k_f = 0.25$ kg/m³s.[18] In all cases, t_{fail} decreases substantially with increasing ΔT, in good agreement with experiment. In both the kinetic and thermodynamic approaches, t_{fail} decreases to a limiting value of approximately 0.1 h. Accordingly, two limiting regimes for t_{fail} are evident in Figure 6. For small subcoolings (i.e., $\Delta T < 3$ K and $\Delta T < 11$

K for thermodynamic and kinetic freezing, respectively), t_{fail} is limited by freezing, whereas for larger subcoolings, t_{fail} is limited by water production. Figure 9 illustrates the latter case. Here, predicted t_{fail} is larger than the time required for ice crystallization (i.e., 40 and 260 s in the cGDL and cCL, respectively), since $S_I < S_{Ifail}$ upon complete crystallization of all liquid water present. S_I increases further to S_{Ifail} only as newly-generated water freezes. In Figure 6, measured and predicted t_{fail} is for a current density, i, of 20 mA/cm². Significantly, our numerical model reveals that current densities greater than 20 mA/cm² likewise exhibit cell-failure times with two limiting regimes, as in Figure 6. Furthermore, t_{fail} decreases monotonically with increasing current density in the water-production-limited regime (i.e., $\Delta T > 11$ K), as discussed elsewhere.[3,6–8,19,38]

In both the cCL and cGDL, $\bar{\tau}_I$ decreases significantly with increasing subcooling (e.g., see Figure 2). Consequently, as subcooling extends beyond $\Delta T = 11$ K, $\bar{\tau}_I$ is negligible in both cell domains, and ice-crystallization kinetics is well approximated by the thermodynamic-based approach. We conclude that including ice-crystallization kinetics is critical in the "nucleation-limited" regime (see Figure 14 of Dursch et al.)[20] where induction times are long (i.e., from $3 \leq \Delta T \leq 10$ K in Figure 6). However, the particular ΔT that establishes the "nucleation-limited" regime relies heavily on all heat transfer and kinetic parameters (e.g., U, U_{eff}, $\bar{k}_T$, and $J(T)$). These controlling parameters can be adjusted to lengthen $\bar{\tau}_I$, significantly delaying or even preventing ice formation.[34]

The ice distribution at cell failure in both the cCL and cGDL depends strongly on subcooling through $\bar{\tau}_{I,cGDL}(T)$ and $\bar{\tau}_{I,cCL}(T)$. Figure 10 displays the ratio of spatially-averaged ice saturation in the cGDL to that in the cCL, $\bar{S}_{I,cGDL}/\bar{S}_{I,cCL}$, as a function of subcooling, ΔT, for $i = 20$ mA/cm². Solid lines are calculated using ice-crystallization kinetics in the BP460 and Vulcan XC72 cCLs and the Toray cGDL. The dashed line is calculated using the previous thermodynamic-based rate expression (see Eq. 1).[18] Similar to t_{fail} in Figure 6, $\bar{S}_{I,cGDL}/\bar{S}_{I,cCL}$ decreases substantially with increasing ΔT in all cases. In both the kinetic and thermodynamic approaches, $\bar{S}_{I,cGDL}/\bar{S}_{I,cCL}$ decreases to a limiting value of approximately 0.6. At these subcoolings (i.e., $\Delta T > 3$K and $\Delta T > 9$ K for thermodynamic and kinetic freezing, respectively), rapid ice crystallization occurs within the cCL, preventing water migration into the cGDL. Accordingly, there are also two limiting regimes for $\bar{S}_{I,cGDL}/\bar{S}_{I,cCL}$ in Figure 10. For small subcoolings (i.e., $\Delta T < 9$ K), $\bar{S}_{I,cGDL}/\bar{S}_{I,cCL}$ is limited by $\bar{\tau}_{I,cGDL}(T)$, whereas for larger subcoolings $\bar{S}_{I,cGDL}/\bar{S}_{I,cCL}$ is limited by $\bar{\tau}_{I,cCL}(T)$. This finding is consistent with Ge et al.,[2] who observed two limiting regimes in an operating PEMFC during cold-start using in-situ visible imaging. Eqs. 4–8 and A1–A6 do not allow

for ice propagation between the cCL and cGDL,[17–19] since the shortest induction time controls cell failure. Accordingly, the two limiting regimes in Figure 10 emphasize the importance of ice-crystallization kinetics in both the cCL and cGDL.

Conclusions

We determine isothermal ice-crystallization rates and ice-nucleation rates from heat-flow and induction-time measurements in fuel-cell catalyst layers using differential scanning calorimetry. Isothermal ice-crystallization rates and ice-nucleation rates are obtained as a function of subcooling for four commercial carbon-support materials, with varying ionomer fraction and platinum loading. Measured induction times follow expected trends from classical nucleation theory and reveal that both the carbon-support material and ionomer fraction considerably impact the rate of ice formation. Conversely, dispersed platinum particles play little role in ice crystallization. Following our previous approach, a nonlinear ice-crystallization rate expression is obtained from Johnson-Mehl-Avrami-Kolmogorov theory.

To validate ice-crystallization kinetics within PEMFCs, we measure cell-failure time as a function of subcooling during isothermal galvanostatic cold-start in a commercial MEA. Significantly, cell-failure time decreases with decreasing temperature due to a shorter required time for ice nucleation. Using a 1D PEMFC isothermal numerical cold-start model, we compare cell-failure times predicted using the newly obtained rate expression to those predicted using a traditional thermodynamic-based approach. Cell-failure times predicted using ice-freezing kinetics are in good agreement with experiment. The PEMFC cold-start model demonstrates that ice-crystallization kinetics is critical when induction times are long (i.e., in the "nucleation-limited" regime for $T > 263$ K). However, the particular temperature that establishes the "nucleation-limited" regime relies heavily on all heat transfer and kinetic parameters. Accordingly, these controlling parameters can be adjusted to lengthen induction times, significantly delaying or even preventing ice formation.

Acknowledgments

List of Symbols

A	ice-nucleation-rate constant (nuclei/m^3/s)
B	ice-nucleation-rate constant (K^3)
$\hat{C}_p$	specific heat capacity (J/g-K)
ΔG^*	Gibbs-free energy of critical-nucleus formation (J)
$\Delta \hat{H}_f$	heat of fusion per mass of solid (kJ/kg)
i	current density (A/m^3)
J	pseudo-steady-state nucleation rate (nuclei/m^3/s)
k	overall crystallization rate constant (s$^{-2.5}$)
k_f	equilibrium freezing rate constant (kg/m^3/s)
k_k	effective permeability of phase k (m^{-2})
k_B	Boltzmann constant (J/molecule/K)
$\bar{k}_T$	constant volume-averaged thermal conductivity (W/m/K)
P_C	capillary pressure, $P_G - P_L$ (Pa)
$\dot{Q}$	heat-flow rate (mW)
r^*	critical-nucleus radius (nm)
R_I	ice-generation rate ((generated ice volume)/(water plus ice volume)/time)
R_S	seed-particle radius (nm)
S	saturation
t	time (s)
t_{fail}	MEA-cell-failure time (s)
T	temperature (K)
T_C	crystallization temperature (K)
ΔT	subcooling (K)
U	overall heat transfer coefficient (W/m^2/K)
U_{eff}	effective overall heat transfer coefficient (W/m^2/K)
V	volume (m^3)
x	denotes partial differentiation

Greek Letters

α	thermal diffusivity (m^2/s)
ε	volume fraction
ε_o	bulk porosity
γ	surface tension (dyne/cm)
η	viscosity (Pa-s)
η_o	dimensionless thermal-growth constant
η_s	surface overpotential (V)
θ	contact angle
Π	Peltier coefficient (V)
ρ	mass density (kg/m^3)
τ_g	time for nuclei grow to an instrument-detectable size (s)
τ_i	isothermal induction time (s)
τ_I	non-isothermal induction time (s)
ϕ	gas-free ice volume fraction
ω	instrument constant, 0.0173
Ψ	heterogeneous nucleation shape factor in Eq. B1

Subscripts

a	anode
c	cathode
G	gas
I	ice
k	phase
L	liquid water
o	initial

Appendix A. PEMFC Cold-Start Continuum Model

Within the cCL and cGDL, we write continuum differential energy and mass conservation balances for gas (G), liquid (L), and ice (I). In each subdomain, phase saturations sum to unity, i.e., $S_G + S_L + S_I = 1$, where the saturation of a phase k, S_k, is defined as volume of phase k per pore volume, or $\varepsilon_k/\varepsilon_o$, where ε_k is porosity of phase k and ε_o is bulk porosity. Upon thermal equilibrium among all phases,[15–19] the 1-D, transient energy balance to calculate transient temperature distributions, $T(x,t)$, in each subdomain is

$$\overline{\rho \hat{C}}_P \frac{\partial T}{\partial t} = \bar{k}_T \frac{\partial^2 T}{\partial x^2} + \rho_I \varepsilon_o \Delta \hat{H}_f (S_L + S_I) R_I + \dot{Q}_{rxn}, \qquad [A1]$$

where $\overline{\rho \hat{C}}_p$ is constant volume-averaged heat capacity, $\bar{k}_T$ is constant volume-averaged thermal conductivity, ρ_I is ice mass density, and R_I is the rate of ice formation ((generated ice volume)/(water plus ice volume)/time).[21] In Eq. A1, $\dot{Q}_{rxn} = i(\eta_s + \Pi)/L_{cCL}$ in the cCL and zero in the cGDL, where i is volumetric current density, η_s is surface overpotential (calculated from measured cell voltage in Figure 5),[40] L_{cCL} is cCL thickness, and Π is the Peltier coefficient.[40] The second and third terms on the right side of Eq. A1 represent enthalpy liberation due to crystallization and reaction, respectively. Because of the low subcoolings used in the calculations, heat generation (or consumption) due to evaporation, condensation, sublimation, and deposition (i.e., frosting) are neglected. Additionally, current density in $\dot{Q}_{rxn}$ increases linearly with increasing S_G, so that higher ice and water saturations choke the electrochemical production of liquid water.[19] More involved models are discussed elsewhere.[15–19]

In each subdomain, gas-, liquid-, and ice-phase saturations obey the following mass-conservation equations combined with Darcy's law[15–19]

$$\varepsilon_o \rho_G \frac{\partial S_G}{\partial t} = \frac{\partial}{\partial x} \left(\frac{\rho_G k_G [S_G]}{\eta_G} \frac{\partial P_G}{\partial x} \right), \qquad [A2]$$

$$\varepsilon_o \rho_L \frac{\partial S_L}{\partial t} = \frac{\partial}{\partial x} \left(\frac{\rho_L k_L [S_L]}{\eta_L} \frac{\partial P_L}{\partial x} \right) - \rho_I \varepsilon_o (S_L + S_I) R_I + R_{rxn} \qquad [A3]$$

and

$$\varepsilon_o \rho_I \frac{\partial S_I}{\partial t} = \rho_I \varepsilon_o (S_L + S_I) R_I \qquad [A4]$$

where $R_{rxn} = i M_{H_2O}/2F$ in the cCL and R_{rxn} equals zero in the cGDL, η is viscosity, P is pressure, M_{H_2O} is the molar mass of water, and $k_k[S_k]$ is the effective permeability of phase k as a function of S_k. The first, second, and third terms on the right of Eq. A3 represent water movement due to a gradient in capillary pressure, $P_C \equiv P_G - P_L$, water depletion due to freezing, and water generation due to reaction, respectively. The effective permeabilities in Eqs. A2 and A3 follow the relation $k_k = k_o S_k^3$, where k_o is absolute permeability.[19] Following others,[15–19] residual saturations are neglected. To relate capillary pressure, $P_C \equiv P_G - P_L$, to liquid saturation, capillary equilibrium (i.e., Young-Laplace) and a bundle-of-capillaries model are used.[41] Capillary pressure-saturation relationships used in this work are identical to those measured by Kusoglu et al.[23] A detailed description of mixed-wettability for the cCL and cGDL is found in Balliet et al.[19]

Appendix B. Ice-Nucleation-Rate Parameters

$\phi(t; T)$ and $\bar{\tau}_i(T)$ in Eqs. 3–5 require independent assessment of the ice/water/substrate triple line contact angle, θ. Since A is independent of θ, $J(T)$ depends on θ only through the parameter B. From CNT, B is related to the Gibbs-free energy of critical-nucleus formation, ΔG^*, by[20,30]

$$B(\theta) = \frac{(\Delta T)^2 \Delta G^*}{k_B} = \frac{4\pi \gamma_{sl}^3 T_o^2 \hat{v}_I^2}{3\Delta \hat{H}_f^2 k_B} g(\theta) \qquad \text{[B1]}$$

where k_B is the Boltzmann constant, γ_{sl} is solid/liquid interfacial energy, and $\hat{v}_I$ is ice specific volume.

From Table I and Eq. B1, similar values of B for BP460/BP800 and a Toray GDL[21] suggests that θ for BP460/BP800 is approximately equal to that of the GDL, or $\theta = 60°$. Unlike BP460/BP800, however, BP120/Vulcan XC72 have significantly decreased ice-nucleation rates (evidenced by larger B in Table I). Values of B are roughly 4 times larger for BP120/Vulcan XC72 than for BP460/BP800, characteristic of an increased contact angle, θ. Eq. B1 demonstrates that B (and ΔG^*) increases with θ. Thus, for an increase in θ from 60° to 110° for BP120/Vulcan XC72, ΔG^* increases by a factor of 4–5, consistent with measured B values. For BP120/Vulcan XC72, a larger θ is conceivably due to an increased coverage of the ionomer, comprised of a non-ice-wetting PTFE backbone.[39] This result is similar to our previous finding where ice nucleation occurs more slowly on hydrophobic PTFE-coated GDL fibers than hydrophilic oxidized-carbon fibers.[20]

To investigate further the effect of ionomer coverage on ice-nucleation, the Carbon:Nafion mass ratio was varied from 5:1 to 5:8 for BP800 and Vulcan XC72. Measured values of A and B, obtained as in the rate-expression section, are listed in Table B1. For BP800, B increases from 10.6 to 43.5 as the Carbon:Nafion mass ratio increases from 5:2 to 5:8. This result suggests an increase in ionomer coverage, and consequently, an increase in θ from 60° to approximately 110°, as for BP120/Vulcan XC72. For Vulcan XC72, however, an increased Carbon:Nafion mass ratio results in no further increase in B (likely due to a smaller particle surface area). Conversely for Vulcan XC72, as the Carbon:Nafion mass ratio is decreased, B decreases significantly from 41.6 to 18.9. This indicates decreased ionomer coverage and, similar to BP800 (with 5:2 Carbon:Nafion), a smaller value of θ.

To account for contributions of curvature and seed-particle (particle serving as a nucleation site, e.g., platinum and carbon) size to ΔG^*, we replace $g(\theta)$ In Eq. B1 with $\Psi^3(\theta, x^*)$ (see Eq. 18.10 in Kashchiev),[31] where $x^* = R_S/r^*(T)$ is the ratio of seed-particle to critical-nucleus radius. For heterogeneous growth of a nucleus on a flat surface, $\Psi^3(\theta, x^*) = g(\theta)$ as expected.[30] Figure B1 shows calculated dimensionless Gibbs-free energy of critical-nucleus formation, $\Delta G^*/k_B T$, versus dimensionless seed-particle radius, $x^* = R_S/r^*(T)$, for $\theta = 60°$ and 110°. Solid and dashed lines denote subcoolings of 12.5 K and 15 K, respectively. Arrows label minimum and maximum x^* for platinum (3–5 nm diameter) and the carbon support (30–50 nm diameter) within the cCLs. Several features are salient. Primary carbon particles are much larger than growing nuclei (ranging from 2–4 nm diameter depending on ΔT). Thus, in this case, $x^* \gg 1$, and nuclei grow as solid segments on a flat surface, similar to those in a GDL.[20,21] Compared to the carbon support, ΔG^* is significantly larger for dispersed platinum. Since platinum particles are similar in size to growing nuclei, a larger surface area is required to maintain a given θ, increasing ΔG^*. As a result, ice nuclei form preferentially on the carbon support,
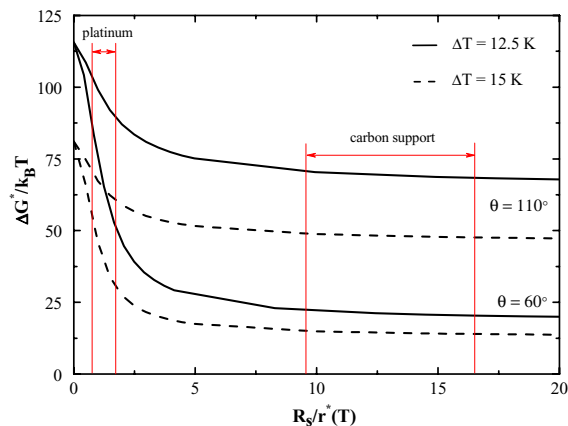

Figure B1. Calculated dimensionless Gibbs-free energy of critical-nucleus formation, $\Delta G^*/k_B T$, versus dimensionless seed radius, $x^* = R_S/r^*(T)$, for ice/water/substrate contact angles of 60° and 110°, where $r^*(T)$ is the radius of a critical nucleus. Solid and dashed lines denote subcoolings of 12.5 K and 15 K, respectively. Arrows establish minimum and maximum dimensionless seed radii calculated for platinum and carbon within the PEMFC catalysts.

in agreement with the $\bar{\tau}_i(T)$ and $\phi(t; T)$ measurements (see Figures 2 and 4). Further, lines in Figure B1 illustrate that ΔG^* (and B) increases with θ as discussed previously.

References

1. E. Cho, J. J. Jo, H. Y. Ha, S. Hong, K. Lee, T. Lim, and I. Oh, *J. Electrochem. Soc.*, **150**, A1667 (2003).
2. S. Ge and C.-Y. Wang, *Electrochem. Sold-State Lett.*, **9**, A499 (2006).
3. K. Tajiri, Y. Tabuchi, F. Kagami, S. Takahashi, K. Yoshizawa, and C. Y. Wang, *J. Power Sources*, **165**, 279 (2007).
4. S. Ge and C. Y. Wang, *J. Electrochem. Soc.*, **154**, B1399 (2007).
5. Y. Hiramitsu, N. Mitsuzawa, K. Okada, and M. Hori, *J. Power Sources*, **195**, 1038 (2010).
6. Y. Hishinuma, T. Chikahisa, F. Kagami, and T. Ogawa, *Japan Soc. Mech. Eng. Intern.*, **47**, 235 (2004).
7. Y. Tabe, M. Saito, K. Fukui, and T. Chikahisa, *J. Power Sources*, **208**, 366 (2012).
8. P. Oberholzer, P. Boillat, R. Siegrist, R. Perego, A. Kästner, E. Lehmann, G. G. Scherer, and A. Wokaun, *J. Electrochem. Soc.*, **159**, B235 (2011).
9. R. Satija, D. L. Jacobson, M. A. Arif, and S. A. Werner, *J. Power Sources*, **129**, 238 (2003).
10. G. Hwang, H. Kim, R. Lujan, R. Mukundan, D. Spernjak, R. L. Borup, M. Kaviany, M. H. Kim, and A. Z. Weber, *Electrochim. Acta*, **95**, 29 (2013).
11. Y. Ishikawa, T. Morita, K. Nakata, K. Yoshida, and M. Shiozawa, *J. Power Sources*, **163**, 708 (2007).
12. Y. Ishikawa, H. Hamada, M. Uehara, and M. Shiozawa, *J. Power Sources*, **179**, 547 (2008).
13. S. Ge and C. Y. Wang, *Electrochim. Acta*, **52**, 4825 (2007).
14. H. Meng, *J. Power Sources*, **178**, 141 (2008).
15. L. Mao, C. Y. Wang, and Y. Tabuchi, *J. Electrochem. Soc.*, **154**, B341 (2007).
16. L. Mao and C. Y. Wang, *J. Electrochem. Soc.*, **154**, B139 (2007).
17. K. Jiao and X. Li, *Electrochim. Acta*, **54**, 6876 (2009).
18. R. Balliet, K. E. Thomas-Alyea, and J. Newman, *ECS Trans.*, **16**, 285 (2008).
19. R. Balliet and J. Newman, *J. Electrochem. Soc.*, **158**, B927 (2011).
20. T. J. Dursch, M. A. Ciontea, C. J. Radke, and A. Z. Weber, *Langmuir*, **28**, 1222 (2012).
21. T. J. Dursch, M. A. Ciontea, G. J. Trigub, C. J. Radke, and A. Z. Weber, *Intl. J. Heat Mass Trans.*, **60**, 450 (2013).
22. D. C. Huang et al., *Int. J. Electrochem. Sci.*, **6**, 2551 (2011).
23. A. Kusoglu, A. Kwong, K. T. Clark, H. P. Gunterman, and A. Z. Weber, *J. Electrochem. Soc.*, **159**, F530 (2012).
24. S. Jiang and J. H. ter Horst, *Cryst. Growth Des.*, **11**, 256 (2011).
25. M. Avrami, *J. Chem. Phys.*, **7**, 1103 (1939).
26. M. Avrami, *J. Chem. Phys.*, **8**, 212 (1940).
27. W. A. Johnson and R. F. Mehl, *AIME Trans.*, **135**, 416 (1939).
28. A. N. Kolmogorov, *Selected Works of A. N. Kolmogorv*, vol. 1, Kluwer Academic Publishers, Dordrecht (1985).
29. D. Kashchiev, D. Verdoes, and G. M. van Rosmalen, *J. Cryst. Growth*, **110**, 373 (1991).
30. U. D. Uhlman and B. Chalmers, *Ind. Eng. Chem.*, **57**, 19 (1965).
31. D. Kashchiev, *Nucleation: Basic Theory with Applications*, Butterworth-Heinemann, Burlington, MA (2000).
32. H. R. Corti, F. Nores-Pondal, and M. P. Buera, *J. Power Sources*, **161**, 799 (2006).

Table B1. Ice-Nucleation Rate Parameters with Varying Carbon:Nafion Mass Ratio.

Catalyst	Carbon:Nafion Mass Ratio	A ($\times 10^{-8}$ nuclei m^{-3} s^{-1})	B ($\times 10^{-4}$ K^3)
Vulcan XC72	5:1	13.3	18.9
	5:2	112.7	40.3
	5:4	103.4	41.6
BP800	5:2	4.6	10.6
	5:4	110.0	17.1
	5:8	305.9	43.5

33. J. Newman and K. E. Thomas Alyea, *Electrochemical Systems*, p. 611, John Wiley & Sons, New York (2004).
34. T. J. Dursch, J. F. Liu, G. J. Trigub, C. J. Radke, and A. Z. Weber, *ECS Trans.*, accepted.
35. T. J. Dursch, J. F. Liu, G. J. Trigub, C. J. Radke, and A. Z. Weber, *Intl. J. Heat Mass Trans.*, **67**, 896 (2013).
36. G. S. Hwang and A. Z. Weber, *J. Electrochem. Soc.*, **159**, F683 (2012).
37. T. Rosén, J. Eller, J. Kang, N. I. Prasianakis, J. Mantzaras, and F. N. Büchi, *J. Electrochem. Soc.*, **159**, F536 (2012).
38. K. Tajiri, Y. Tabuchi, and C-Y Wang, *J. Electrochem. Soc.*, **154**, B147 (2007).
39. X. Li, F. Feng, K. Zhang, S. Ye, D. Kwok, and V. Birss, *Langmuir*, **28**, 6698 (2012).
40. A. Z. Weber and J. Newman, *Chem. Rev.*, **104**, 4679 (2004).
41. A. Z. Weber, *J. Power Sources*, **195**, 5292 (2010).